Prediction of traffic oscillation instability with spectral analysis of the Aw-Rascle-Zhang model

Authors[a]

[a]address

Abstract

Keywords:

1. Introduction

Around the world traffic congestion causes a drain on the economy due to time and fuel wasted and collisions associated with traffic congestion. In 2011 congestion in America alone caused a loss of \$121 billion due to 5.5 billion hours of extra travel time and 2.9 billion gallons of wasted fuel. Although congestion levels in America are much higher now than several decades ago, they have dropped below the peak in 2005, but will increase when the economy improves[1]. As personal vehicle ownership increases globally, traffic congestion continues to be a persistent problem. It is no surprise then that research in the physics of traffic is developed with the ultimate goal of mitigating road traffic. Traffic control strategies such as ramp metering and variable speed limits are in place today, but a good model of traffic dynamics is needed for proper coordination of control strategies.

1.1. First order models

The topic of traffic models is vast, ranging from dense arterial networks to freeways spanning across the continent. In this article we focus on homogeneous road sections, in particular no ramps or intersections are present. The 1950's saw the development of the Lighthill-Whitham-Richards (LWR) model [2, 3], which became the seminal model for traffic flow, still studied today. This model is a conservation law for vehicles, based on fluid dynamics. Let ρ the lineic vehicular density (veh/m) and q the traffic flux (veh/s), dynamics follow the equation $\frac{\partial \rho}{\partial t} + \frac{\partial q}{\partial x} = 0$. The simplicity of the model enabled the formulation of numerical discretization schemes such as Godunov ([4, 5]) or cell transmission models ([6, 7]). These are used in everyday transportation research (e.g. Berkeley Advanced Traffic Simulation system).

Yet as a first-order model it has inherent shortcomings. Most of these have been pointed out in [8]. The LWR model fails to describe accurately what happens when a vehicle crosses a shock. Although the Rankine-Hugoniot condition guarantees macroscopic mass conservation, at the microscopic scale the speed of traveling particle would be unrealistically discontinuous. It is also well known that this first order model fails to predict light traffic dynamics in a sensible manner. Considering all drivers are identical is contradictory with platoons dissolving because users' desired speeds vary from one person to another. Also stop and go behavior otherwise named traffic oscillations cannot appear in the model with expanding amplitudes although this phenomenon is observed in practice. This phenomenon has attracted more an more attention in transportation research. Jamitons, traffic jam that appears without the presence of a bottleneck have been reproduced in small experiments ([9, 10]) and explained theoretically as the result of a particular configuration of the traffic system ([11]) as well as an outcome of fuzzy fundamental diagrams ([12]). Empirical studies have focused on detecting and quantifying this effect ([13]) on actual freeways in day-to-day traffic. Car-following behaviors ([14]) and lane-changing ([15, 16]) are often seen as the cause of oscillations. Several approaches have been developed in order to model these empirical facts.

1.2. First generation second order models

This article will focus on macroscopic second order models as opposed to microscopic and mesoscopic frameworks. Payne and Whitham have developed in parallel an identical system of equations that aimed at a finer traffic modeling ([17, 18]). Their main objective was describing in details what happens inside a traffic shock. To that end, they followed the same approach as in fluid dynamics and used a higher order model that would capture momentum related features. The Payne-Whitham model (PW) therefore consists of a mass conservation equation identical to that of LWR seconded by a momentum equation $\frac{\partial v}{\partial t} + v \frac{\partial v}{\partial x} + \frac{p'(\rho)}{\rho} \frac{\partial \rho}{\partial x} = \frac{V(\rho) - v}{\tau} + \nu \frac{\partial^2 v}{\partial x^2}$ where the pressure function p is strictly increasing and the speed equilibrium V is decreasing. As Daganzo pointed later in his review of second order models ([8]), this approach was flawed both in the derivation of its equations and its predictions. The formulation of PW relies on the assumption that spacing and speed vary slowly which would yield negligible 2nd and 3rd derivatives for these quantities. This is contradictory with the observations of Newell ([19]) where his car following model predicts sharp and quick changes in these quantities. In terms of physics, modeling traffic as a gas was highly unrealistic as fluids feature an anisotropic propagation of the information. Things are very different with traffic where cars will mostly react to downstream conditions. This is incompatible with the slope of one of the characteristic lines being greater than cars' speeds in the PW model. Also, at the upstream end of a jam with low density, traffic would flow in reverse if $\nu \neq 0$ which is completely unrealistic. Finally, gas particles are physically identical whereas drivers have different habits and desired speeds. The heterogeneous composition of traffic is not taken into account in the PW model, hence another flaw.

1.3. Second generation second order models

After this requiem, second order traffic models where not forgotten though. Zhang improved the mathematical structure of his first model ([20]). At first it was highly similar to that of PW in its momentum equation $\frac{\partial v}{\partial t} + v \frac{\partial v}{\partial x} + \rho \left(V_*'(\rho) \right)^2 \frac{\partial \rho}{\partial x} = \frac{V(\rho) - v}{\tau}$ where $\rho V_*'(\rho)$ represents the information propagation speed in traffic. This improvement was conducted independently of Aw and Rascle's work and eventually gave birth to an identical model (ARZ) ([21, 22]). The second order equation in that model, $\frac{\partial(v + p(\rho))}{\partial t} + v \frac{\partial(v + p(\rho))}{\partial x} = \frac{\rho(V(\rho) - v)}{\tau}$, does not present any wrong way travels. Indeed it corresponds to a setup of the PW model where $\nu = 0$. Also, it does not feature any gas-like behavior that contradicts the elementary physics of traffic. The key element for the model was formulating the evolution of the pseudo-pressure term $v + p(\rho)$ in a convective manner. This indeed changed the information propagation from a gas-like anisotropic behavior to a quantity that would be carried by the particles in the system at speed v. This model has since been thoroughly studied. [21] concluded that a relaxation term accounting for traffic equilibrium was needed so the speed of cars would be determined by the fundamental diagram and not the initial data. The effect of the relaxation has been studied in [23] where the author proved that, interestingly, the relaxed model converges towards LWR when $\tau \to 0$. It has been showed in [24] that the first ARZ model needed a fundamental diagram extended for negative and maximum speeds, zero and maximum densities so as to guarantee solutions to the Riemann and stability with low densities. In [25] discretization enabled extending the AR model to a network setup with junctions and traffic lights. The ARZ model now has a legacy that started with the extended ARZ model ([26]). An extension was presented in [27] as a pressure-less limit of the AR model where drivers will not significantly slow down if the congestion is not heavy. More recently a generalized model has been created ([28]) that corrects the fact that, in the ARZ model, several maximum densities co-exist which seems contradictory with the fact that this quantity is uniquely determined by the characteristics of the freeway. Finally, a Godunov descretization scheme has been exhibited for the ARZ model in [29]. With an extended fundamental diagram, this framework was able to solve numerically the equations for any Riemann problem. This opened the way to a numerical comparison where ARZ fitted the data better than LWR.

1.4. Models suited for control

It has been remarked in [28] that for congested regimes LWR tends to offer a slightly better fit that ARZ with respect to empirical measurements and is outperformed for low densities. Our aim here is using a model that is suitable for all regimes so as to establish generic control strategies for traffic. The second order model manages to account for traffic oscillations in dense traffic realistically ([30]) hence our electing it. Laplace transform and spectral analysis are powerful tools for control problems that provide a simple

yet holistic represent of a system. In that regard, it is important to have a model that predicts oscillatory phenomena. Models other than second order macroscopic could have been chosen. Behavioral models such as [19] and more recently [31] depict in a detailed fashion the effects of car-following and lane changing on freeway dynamics. Unfortunately their formulation makes them hard to use for control purposes. Recent data driven approaches ([32]) that have tried to model spectral features of traffic thanks to wavelet transform are also not suitable. They are mostly heuristic in that they do not focus on the dynamics core to the system.

1.5. Similarities with Saint-Venant equations

Our control analysis of the ARZ equations is strongly inspired by the analysis of Saint-Venant equations in [33]. Let v the fluid velocity in a canal, q the flux, T the top width and y the water height. One has a mass conservation equation similar to LWR ($T\frac{\partial y}{\partial t} + \frac{\partial Q}{\partial x} = 0$) and a momentum equation structurally similar to ARZ ($\frac{\partial v}{\partial t} + v\frac{\partial V}{\partial x} + g\frac{\partial y}{\partial x} = g\left(S_b - S_f\left(x,t\right)\right)$). $S_b - S_f\left(x,t\right)$ is a friction slope equilibrium equation analogous to $\frac{V(\rho)-v}{\tau}$. Linearizing this system about an equilibrium point enabled the design of efficient control strategies for canals leveraging the realism of Saint-Venant equations and the elegance of spectral analysis for linear systems. Approximations for the low frequency domain decompose the transfer matrix into a combination of delay and integration components. This leads to setting up efficient PI controllers while enabling a simpler theoretical analysis of the hydraulic system.

1.6. Approach and contributions

This article will follow the steps taken in ([33]) and adapt them to the analogous ARZ equations so as to achieve a two-fold objective. First we aim at developing strategies that enforce the readability and easiness of use of the ARZ model. Solutions to these non-linear equations are practically hard to derive in an analytical manner. Linearizing the system about an equilibrium is therefore a sound strategy that opens the way to efficient control schemes with multiple inputs and outputs. Although theoretically close, hydrodynamics and traffic belong to different contexts. It will therefore be necessary, in particular when considering the formulation of boundary conditions, to carefully guarantee the well-posedness of the problem. The other objective is assessing the fit quality of the model by practically comparing its output with actual data collected as part of the NGSIM project.

The first main contribution of the article is therefore deriving the linearized equations of the ARZ model in a format that highlights the main properties the model should feature. An equivalent of the Froude in hydrodynamics number is created for traffic that separates free-flowing and congested regimes. The linear system will be diagonalized which provides a very easy to use set of equations for the Riemann invariants. Deriving time domain responses after formulating spectral transfer matrices will prove that the linearized system is unstable in the free-flowing regime and accounts for non-linear wave propagation giving rise to jamitons. An important contribution here is that these waves occur for an entire set of values of velocity, density and flux and lead the linearized system away from its equilibrium point in free-flowing regime. We will show that the spectral form we obtain is a formulation of a second order model consistent with the fact that information does not propagate faster than cars travel. In order to guarantee that linearization does not destroy the realistic properties of ARZ a numerical experiment is conducted. NGSIM data has been used previously so as to assess the quality of second order models' predictions ([29, 28]). However these studies focus on averaged errors and only display predictions at a couple of points on the freeway. Here we show an entire map of the states and conduct the model assessment in a holistic manner. This yields a complete analysis of the strengths and weaknesses of the model that would be used for control. The estimation procedure, unlike [28], does not rely on any assumption about the typical vehicle length or the safety distance factor. The whole procedure is validated by comparing estimates based on independent data features. It is also described how in a linear system, Fast Fourier transform allows fast and simple numerical resolution for most boundary conditions. With this new prediction technique, no discretization scheme is needed and no grid size condition needs to be fulfilled. This procedure will prove that the linearized model successfully accounts for traffic oscillations and will also provide simple and consistent methods to calibrate the τ parameter of the model.

The article is organized in two sections. The first one derives the linearized ARZ equation and their spectral domain form. It shows that this procedure can be conducted for any of the (v, q), (ρ, q), (ρ, v) couple of variables. Velocity and flux being the easiest values that can be observed and controlled in traffic, we will mainly focus on that representation and its diagonalized form. Conditions distinguishing regimes will be highlighted and the traffic Froude number exhibited. We will then derive distributed transfer matrices and analyze their properties thanks to Bode plots. The numerical analysis will be conducted in the second section. After presenting the data, estimation procedures for (v, q, ρ) and the parameters of the model, this study will confront empirical estimates with the numerical values predicted by the linearized model. We will explain how decomposing boundary input signals into fundamental elements thanks to the Fast Fourier Transform turns the spectral domain diagonalized form into a prediction tool.

2. The ARZ model

Aw and Rascle [21] and Zhang [22] independently developed a macroscopic second-order model of traffic flow to address the shortcomings of previously existing higher-order models. The (AR) model proposed by Aw and Rascle consists of the usual vehicle conservation and momentum equations:

$$\rho_t + (\rho v)_x = 0, \tag{1}$$

$$(v + p(\rho))_t + v(v + p(\rho))_x = 0, \tag{2}$$

where $v(x, t)$ and $\rho(x, t)$ are the density and velocity, respectively, and $p(\rho)$ is a smooth, increasing function analogous to the pressure term in fluid flow. Aw and Rascle demonstrate in [21] that "with a suitable choice of function p," the above class of models avoids inconsistencies of earlier second-order models. Zhang proposed in [22] the same model with $p(\rho) = -V(\rho)$, where $V(\rho) = Q(\rho)/\rho$ is the equilibrium velocity profile, and $Q(\rho)$ is the density-flow relation given by the fundamental diagram. In this paper we consider the Aw-Rascle-Zhang (ARZ) model with a relaxation term:

$$\rho_t + (\rho v)_x = 0, \tag{3}$$

$$(v + p(\rho))_t + v(v + p(\rho))_x = \frac{V(\rho) - v}{\tau}, \tag{4}$$

where τ is the relaxation time. Without the relaxation term cars never reach the maximum allowable speed [23]. Note that at the equilibrium velocity this term is zero.

In vector form the ARZ model is

$$\begin{pmatrix} \rho \\ v \end{pmatrix}_t + \begin{pmatrix} v & \rho \\ 0 & v + \rho V'(\rho) \end{pmatrix} \begin{pmatrix} \rho \\ v \end{pmatrix}_x = \begin{pmatrix} 0 \\ \dfrac{V(\rho) - v}{\tau} \end{pmatrix}. \tag{5}$$

With the appropriate variable change, we can rewrite the model in the denisty-flow and velocity-flow forms, the latter of which is most useful to us for practical control purposes. Using the flow relation $q = \rho v$ and (5), the density-flow form is

$$\begin{pmatrix} \rho \\ q \end{pmatrix}_t + \begin{pmatrix} 0 & 1 \\ -\frac{q}{\rho}\left(\frac{q}{\rho} + \rho V'(\rho)\right) & 2\frac{q}{\rho} + \rho V'(\rho) \end{pmatrix} \begin{pmatrix} \rho \\ q \end{pmatrix}_x = \begin{pmatrix} 0 & 0 \\ \frac{V(\rho)}{\tau} & -\frac{1}{\tau} \end{pmatrix} \begin{pmatrix} \rho \\ q \end{pmatrix}. \tag{6}$$

In the same manner we arrive at the velocity-flow form,

$$\begin{pmatrix} v \\ q \end{pmatrix}_t + \begin{pmatrix} v + \frac{q}{v} V'\left(\frac{q}{v}\right) & 0 \\ \frac{q}{v}\left(v + \frac{q}{v} V'\left(\frac{q}{v}\right)\right) & v \end{pmatrix} \begin{pmatrix} v \\ q \end{pmatrix}_x = \frac{1}{\tau} \begin{pmatrix} V\left(\frac{q}{v}\right) - v \\ \frac{q}{v} V\left(\frac{q}{v}\right) - q \end{pmatrix}. \tag{7}$$

2.1. Linearization

We are interested only in small deviations, $(\tilde{\rho}(x,t), \tilde{v}(x,t))$, from the equilibrium. Consider the steady flow solution $(\rho^*(x), v^*(x))(V(\rho^*) = v^*)$. Then (5) becomes

$$v^* \frac{d\rho^*}{dx} + \frac{dv^*}{dx}\rho^* = 0, \tag{8}$$

$$(v^* + \rho^* V'(\rho^*))\frac{dv^*}{dx} = \frac{V(\rho^*) - v^*}{\tau} = 0. \tag{9}$$

We must have $\frac{dv^*}{dx} = 0$ else $v^* + \rho^* V'(\rho^*) = 0$. Then we have also $\frac{d\rho^*}{dx} = 0$. Hence the steady-state solution is uniform along the road.

We linearize the ARZ model (5) about the steady-state described above. We obtain the linearized system

$$\begin{pmatrix} \tilde{\rho} \\ \tilde{v} \end{pmatrix}_t + \begin{pmatrix} v^* & \rho^* \\ 0 & v^* + \rho^* V'(\rho^*) \end{pmatrix}\begin{pmatrix} \tilde{\rho} \\ \tilde{v} \end{pmatrix}_x = \begin{pmatrix} 0 & 0 \\ \frac{V'(\rho^*)}{\tau} & -\frac{1}{\tau} \end{pmatrix}\begin{pmatrix} \tilde{\rho} \\ \tilde{v} \end{pmatrix} \tag{10}$$

Similarly for the density-flow system (6), we linearize about the equilibrium $(\rho^*, q^*)(\rho^* V(\rho^*) = q^*)$ with deviations $(\tilde{\rho}(x,t), \tilde{q}(x,t))$. The linearized system is as follows

$$\begin{pmatrix} \tilde{\rho} \\ \tilde{q} \end{pmatrix}_t + \begin{pmatrix} 0 & 1 \\ \alpha^* \beta^* & \alpha^* - \beta^* \end{pmatrix}\begin{pmatrix} \tilde{\rho} \\ \tilde{q} \end{pmatrix}_x = \begin{pmatrix} 0 & 0 \\ \delta & \sigma \end{pmatrix}\begin{pmatrix} \tilde{\rho} \\ \tilde{q} \end{pmatrix}, \tag{11}$$

where $\alpha^* = \frac{q^*}{\rho^*}$, $\beta^* = -\frac{q^*}{\rho^*} - \rho^* V'(\rho^*)$, $\delta = \frac{V(\rho^*) + \rho^* V'(\rho^*)}{\tau}$, and $\sigma = -\frac{1}{\tau}$.

Finally, for the velocity-flow system,

$$\begin{pmatrix} \tilde{v} \\ \tilde{q} \end{pmatrix}_t + \begin{pmatrix} v^* + \frac{q^*}{v^*}V'\left(\frac{q^*}{v^*}\right) & 0 \\ \frac{q^*}{v^*}\left(v^* + \frac{q^*}{v^*}V'\left(\frac{q^*}{v^*}\right)\right) & v^* \end{pmatrix}\begin{pmatrix} \tilde{v} \\ \tilde{q} \end{pmatrix}_x = \begin{pmatrix} -\dfrac{(v^*)^2 + q^* V'\left(\frac{q^*}{v^*}\right)}{(v^*)^2 \tau} & \dfrac{V'\left(\frac{q^*}{v^*}\right)}{v^* \tau} \\ -\dfrac{q^*\left((v^*)^2 + q^* V'\left(\frac{q^*}{v^*}\right)\right)}{(v^*)^3 \tau} & \dfrac{q^* V'\left(\frac{q^*}{v^*}\right)}{(v^*)^2 \tau} \end{pmatrix}\begin{pmatrix} \tilde{v} \\ \tilde{q} \end{pmatrix}. \tag{12}$$

2.2. Characteristic form

We rewrite the model in the characteristic form by diagonalizing the linearized equations. We begin with the density-flow system. Manipulating the equations in (10), we find

$$\begin{pmatrix} \zeta_1 \\ \zeta_2 \end{pmatrix}_t + \begin{pmatrix} \lambda_1 & 0 \\ 0 & \lambda_2 \end{pmatrix}\begin{pmatrix} \zeta_1 \\ \zeta_2 \end{pmatrix}_x = \begin{pmatrix} -\frac{1}{\tau} & 0 \\ -\frac{1}{\tau} & 0 \end{pmatrix}\begin{pmatrix} \zeta_1 \\ \zeta_2 \end{pmatrix}, \tag{13}$$

where $\zeta_1 = \tilde{v} - V'(\rho^*)\tilde{\rho}$ and $\zeta_2 = \tilde{v}$ are the characteristic variables of the (ρ, v) system, and $\lambda_1 = v^*$ and $\lambda_2 = v^* + \rho^* V'(\rho^*)$ are the eigenvalues. Note that $V'(\rho^*) < 0$ so $\lambda_2 \leq \lambda_1 = v^*$. Therefore this is consistent with the physical dynamics of the system as no waves travel faster than the equilibrium car speed.

We proceed in the same manner above to diagonalize the (ρ, q) system (11). The diagonal form is

$$\begin{pmatrix} \chi_1 \\ \chi_2 \end{pmatrix}_t + \begin{pmatrix} \lambda_1 & 0 \\ 0 & \lambda_2 \end{pmatrix}\begin{pmatrix} \chi_1 \\ \chi_2 \end{pmatrix}_x = \begin{pmatrix} -\frac{1}{\tau} & 0 \\ -\frac{1}{\tau} & 0 \end{pmatrix}\begin{pmatrix} \chi_1 \\ \chi_2 \end{pmatrix}, \tag{14}$$

where $\chi_1 = -\lambda_2 \tilde{\rho} + \tilde{q}$ and $\chi_2 = -\lambda_1 \tilde{\rho} + \tilde{q}$ are the characteristic variables in the (ρ, q) system and the eigenvalues λ_1 and λ_2 are the same as in the density-velocity system due to the relation $q^* = \rho^* v^*$.

Diagonalization of the velocity-flow system is more involved. Letting $\xi(x,t) = (\tilde{v}, \tilde{q})^T$, we can rewrite (12) as

$$\eta_t + A\eta_x = B\eta. \tag{15}$$

The eigenvalues of A are $\lambda_1 = v^*$ and $\lambda_2 = v^* + \frac{q^*}{v^*}V'\left(\frac{q^*}{v^*}\right)$, consistent with the previous systems. Then A can be diagonalized as follows

$$A = XDX^{-1}, \tag{16}$$

$$X = \begin{pmatrix} 0 & \lambda_2 - \lambda_1 \\ 1 & \rho^*\lambda_2 \end{pmatrix}, \tag{17}$$

$$D = \begin{pmatrix} \lambda_1 & 0 \\ 0 & \lambda_2 \end{pmatrix}, \tag{18}$$

$$X^{-1} = \begin{pmatrix} \dfrac{\rho^*\lambda_2}{\lambda_1 - \lambda_2} & 1 \\ -\dfrac{1}{\lambda_1 - \lambda_2} & 0 \end{pmatrix}. \tag{19}$$

Define $\gamma(x,t) := X\eta(x,t)$. Hence (15) can be rewritten as

$$\gamma_t + \begin{pmatrix} \lambda_1 & 0 \\ 0 & \lambda_2 \end{pmatrix}\gamma_x = \begin{pmatrix} -\frac{1}{\bar{t}} & 0 \\ -\frac{1}{q^*\tau} & 0 \end{pmatrix}\gamma \tag{20}$$

where

$$\gamma = \begin{pmatrix} \frac{\rho^*\lambda_2}{\lambda_1 - \lambda_2}\tilde{v} + \tilde{q} \\ -\frac{1}{\lambda_1 - \lambda_2}\tilde{v} \end{pmatrix}. \tag{21}$$

Let $\xi = (\chi_1, -q^*\chi_2)^T$. Then we have

$$\xi_t + \begin{pmatrix} \lambda_1 & 0 \\ 0 & \lambda_2 \end{pmatrix}\xi_x = \begin{pmatrix} -\frac{1}{\bar{t}} & 0 \\ -\frac{1}{\tau} & 0 \end{pmatrix}\xi, \tag{22}$$

and

$$\xi = \begin{pmatrix} \frac{\rho^*\lambda_2}{\lambda_1 - \lambda_2}\tilde{v} + \tilde{q} \\ \frac{q^*}{\lambda_1 - \lambda_2}\tilde{v} \end{pmatrix} = \begin{pmatrix} \frac{\rho^*\lambda_2}{\lambda_1 - \lambda_2} & 1 \\ \frac{\rho^*\lambda_1}{\lambda_1 - \lambda_2} & 0 \end{pmatrix}\begin{pmatrix} \tilde{v} \\ \tilde{q} \end{pmatrix} \tag{23}$$

2.3. "Froude number"

In fluid mechanics the Froude number is a dimensionless number which delineates the boundary between flow regimes. Using the eigenvalues of the system in the characteristic form, we are able to define a useful analog to this number. Since $V(\rho)$ is nonincreasing function we have $V'(\rho^*) \leq 0$. Thus there are two flow regimes, where $\lambda_1\lambda_2 < 0$ and one characteristic curve travels downstream, and where $\lambda_1\lambda_2 > 0$ and both characteristic curves travel upstream.

Define $F := \dfrac{\rho^*V'(\rho^*)}{v^*}$. Then we have

$$\begin{cases} F > 1 & \Rightarrow |\rho^*V'(\rho^*)| > v^* & \Rightarrow \lambda_2 < 0 \\ F < 1 & \Rightarrow |\rho^*V'(\rho^*)| < v^* & \Rightarrow \lambda_2 > 0 \end{cases}.$$

Note also that $\lambda_2 = v^* + \rho^*V'(\rho^*) = \dfrac{Q(\rho^*)}{\rho^*} + \dfrac{\rho^*Q'(\rho^*) - Q(\rho^*)}{\rho^*} = Q'(\rho^*)$. Hence the system is in free flow when $F < 1$ and congestion when $F > 1$.

3. Frequency domain analysis

We consider only the (v,q) system for the frequency domain analysis for practical control purposes as described above.

3.1. State-transition matrix

In this section we analyze the linearized ARZ model in the frequency domain. For control purposes we are most interested in the (v, q) system.

Working with the (22) we obtain the following ODE

$$\frac{\partial \hat{\zeta}(x, s)}{\partial x} = \mathscr{A}(s)\hat{\zeta}(x, s) + \mathscr{B}\zeta(x, t = 0^-), \tag{24}$$

where $\mathscr{A}(s) = A^{-1}(B - sI)$ and $\mathscr{B} = -A^{-1}$. The general solution is

$$\hat{\zeta}(x, s) = \Phi(x, s)\hat{\zeta}(0, s) + \Phi(x, s)\int_0^x \Phi(v, s)^{-1}\mathscr{B}\zeta(v, 0^-)dv, \tag{25}$$

where $\Phi(x, s) = e^{\mathscr{A}(s)x}$ is the state-transition matrix. Assuming zero initial conditions we have

$$\hat{\zeta}(x, s) = \Phi(x, s)\hat{\zeta}(0, s). \tag{26}$$

To compute the exponential we diagonalize the matrix as

$$\mathscr{A}(s) = \mathscr{X}(s)\mathscr{D}(s)\mathscr{X}^{-1}(s) \tag{27}$$

where

$$\mathscr{X}(s) = \begin{pmatrix} 0 & \dfrac{\lambda_2 - (\lambda_1 - \lambda_2)\tau s}{\lambda_1} \\ 1 & 1 \end{pmatrix}, \tag{28}$$

$$\mathscr{D}(s) = \begin{pmatrix} -\dfrac{s}{\lambda_2} & 0 \\ 0 & -\dfrac{1+\tau s}{\tau \lambda_1} \end{pmatrix}. \tag{29}$$

Hence

$$\Phi(x, s) = \mathscr{X}^{-1}(s)e^{\mathscr{D}(s)x}\mathscr{X}(s) = \begin{pmatrix} \phi_{11}(x, s) & \phi_{12}(x, s) \\ \phi_{21}(x, s) & \phi_{22}(x, s) \end{pmatrix}, \tag{30}$$

with

$$\phi_{11} = e^{-\frac{x}{\tau\lambda_1}}e^{-\frac{x}{\lambda_1}s}, \tag{31a}$$

$$\phi_{12} = 0, \tag{31b}$$

$$\phi_{21} = \frac{\lambda_1\left(e^{-\frac{x}{\tau\lambda_1}}e^{-\frac{x}{\lambda_1}s} - e^{-\frac{x}{\lambda_2}s}\right)}{\lambda_2 - \tau(\lambda_1 - \lambda_2)s}, \tag{31c}$$

$$\phi_{22} = e^{-\frac{x}{\lambda_2}s}. \tag{31d}$$

3.2. Free flow case

Consider the system in the free flow regime. From (22) we see that ζ_1 travels with characteristic speed λ_1 and ζ_2 with characteristic speed λ_2. In the free flow regime we have $\lambda_1 \geq \lambda_2 > 0$, hence two boundary conditions are needed, both at the upstream boundary. A plot of the characteristics is shown in Figure 1.
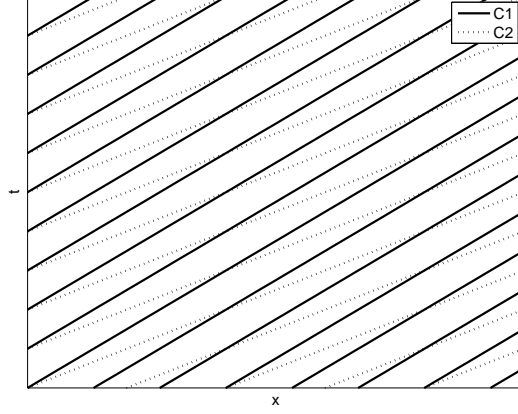
Figure 1: Illustration of the characteristics for supercritical flow, $\lambda_1 \geq \lambda_2 > 0$.

With $\zeta_1(0, t)$ and $\zeta_2(0, t)$ as the inputs and $\zeta_1(L, t)$ and $\zeta_2(L, t)$ as the outputs, the distributed transfer matrix is exactly the state-transition matrix $\Phi(x, s)$.

Using (23), we can write

$$
\begin{pmatrix} \widetilde{v}(x, s) \\ \widetilde{q}(x, s) \end{pmatrix} = \underbrace{\begin{pmatrix} \dfrac{\rho^* \lambda_2}{\lambda_1 - \lambda_2} & 1 \\ \dfrac{\rho^* \lambda_1}{\lambda_1 - \lambda_2} & 0 \end{pmatrix}^{-1} \Phi(x, s) \begin{pmatrix} \dfrac{\rho^* \lambda_2}{\lambda_1 - \lambda_2} & 1 \\ \dfrac{\rho^* \lambda_1}{\lambda_1 - \lambda_2} & 0 \end{pmatrix}}_{\Psi(x, s)} \begin{pmatrix} \widetilde{v}(0, s) \\ \widetilde{q}(0, s) \end{pmatrix} \tag{32}
$$

with

$$
\psi_{11}(x, s) = \left(e^{-\frac{x}{\lambda_1 \tau}} e^{-\frac{x}{\lambda_1} s} - e^{-\frac{x}{\lambda_2} s} \right) \frac{\alpha}{s + \alpha} + e^{-\frac{x}{\lambda_2} s}, \tag{33a}
$$

$$
\psi_{12}(x, s) = -\frac{1}{\rho^* \tau} \left(e^{-\frac{x}{\lambda_1 \tau}} e^{-\frac{x}{\lambda_1} s} - e^{-\frac{x}{\lambda_2} s} \right) \frac{1}{s + \alpha}, \tag{33b}
$$

$$
\psi_{21}(x, s) = -\rho^* \tau \left(e^{-\frac{x}{\lambda_1 \tau}} e^{-\frac{x}{\lambda_1} s} - e^{-\frac{x}{\lambda_2} s} \right) \frac{\alpha s}{s + \alpha}, \tag{33c}
$$

$$
\psi_{22}(x, s) = -\left(e^{-\frac{x}{\lambda_1 \tau}} e^{-\frac{x}{\lambda_1} s} - e^{-\frac{x}{\lambda_2} s} \right) \frac{\alpha}{s + \alpha} + e^{-\frac{x}{\lambda_1 \tau}} e^{-\frac{x}{\lambda_1} s}. \tag{33d}
$$

where $\alpha = -\dfrac{\lambda_2}{\tau(\lambda_1 - \lambda_2)}$.

3.2.1. Bode plots

We generate Bode plots using the following parameters taken from [34]: $q_{max} = 1300$ veh/h, $\rho_{max} = 0.1$ veh/m, and $L = 100$ m: The Greenshields Hamiltonian, $Q(\rho) = 4 \frac{q_{max}}{\rho_{max}^2} \rho(\rho_{max} - \rho)$, is used to approximate the fundamental diagram. For inhomogenous second-order models, the relaxation time, τ, falls in the range of about 14-60 seconds [28]. A relaxation time of $\tau = 15$ s is used for the following simulations. We simulate for $\rho^* = 0.01$.

The Bode plots for the physical variables are display on Figure 2 and Figure 3. For the Riemann invariants only $\phi_{21}(x, s)$ and $\phi_{22}(x, s)$ are represented on Figure 4 and Figure 5 ($\phi_{11}(x, s)$ and $\phi_{12}(x, s)$ are only delay functions).
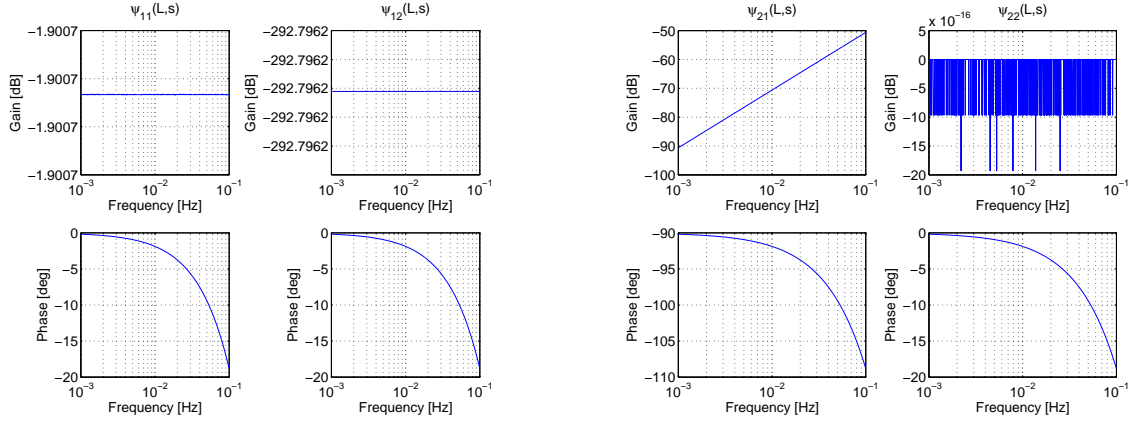
8

Figure 2: Magnitude and phase bode plots for $\psi_{11}(L,s)$ and $\psi_{12}(L,s)$ (left) and for $\psi_{21}(L,s)$ and $\psi_{22}(L,s)$ (right). (Physical variables)
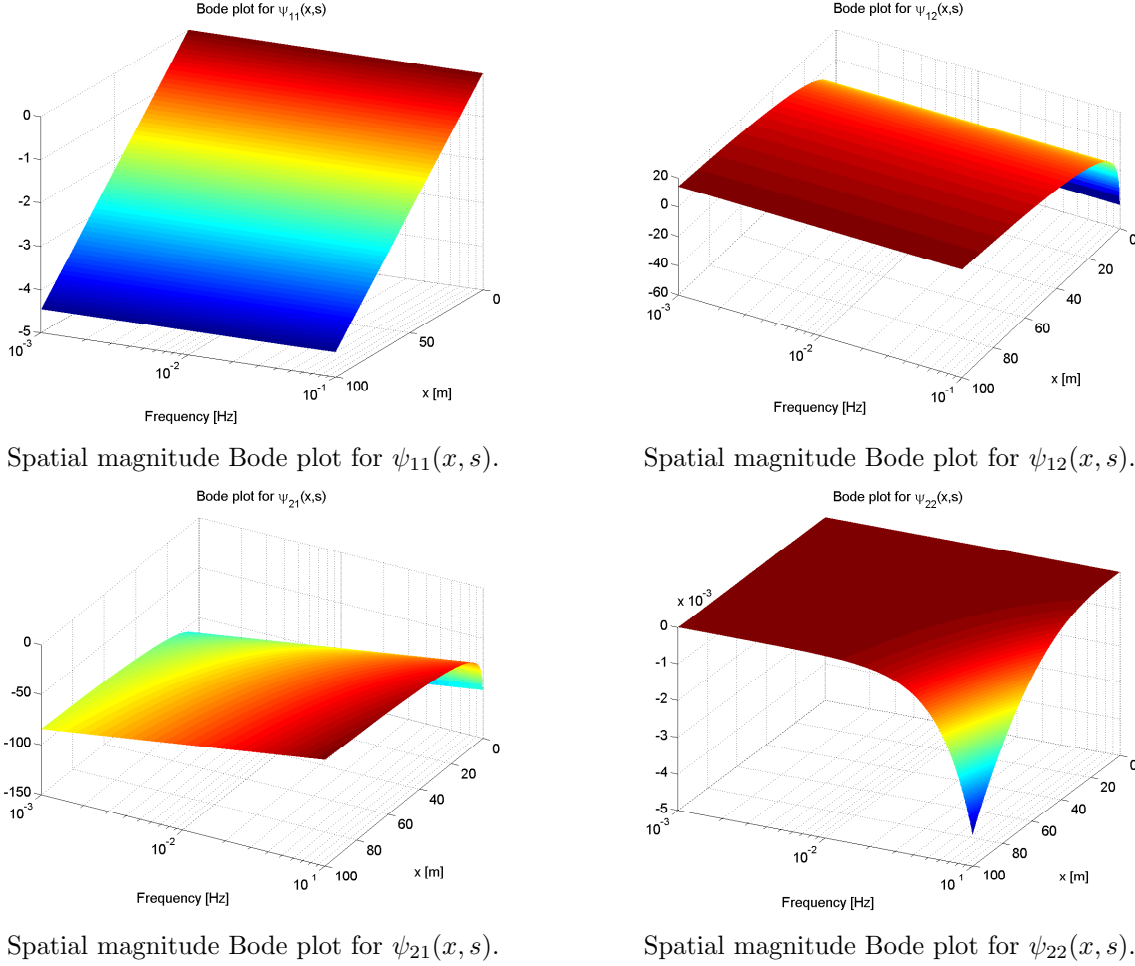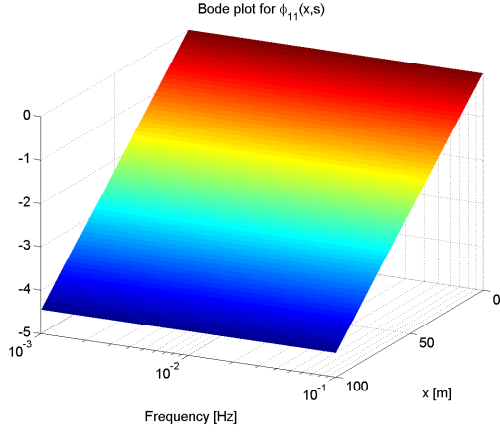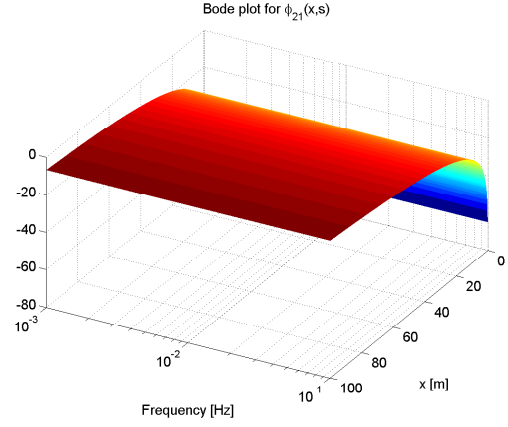

Spatial magnitude Bode plot for $\psi_{11}(x,s)$.

Spatial magnitude Bode plot for $\psi_{12}(x,s)$.

Spatial magnitude Bode plot for $\psi_{21}(x,s)$.

Spatial magnitude Bode plot for $\psi_{22}(x,s)$.

Figure 3: Spatial magnitude Bode plots for physical variables

9

Bode plot for $\phi_{11}(x,s)$

Bode plot for $\phi_{21}(x,s)$

Spatial magnitude Bode plot for $\phi_{21}(x,s)$.

Spatial magnitude Bode plot for $\phi_{22}(x,s)$.

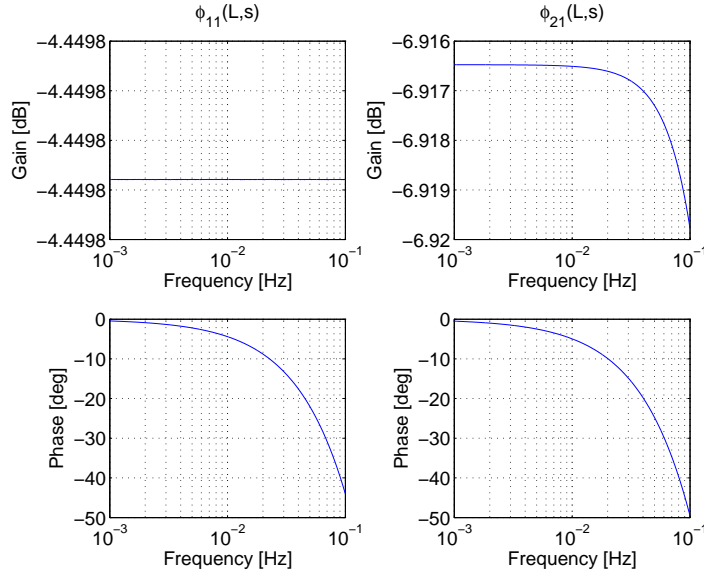Figure 5: Spatial magnitude Bode plots for Riemann invariants

$\phi_{11}(L,s)$

$\phi_{21}(L,s)$

Figure 4: Magnitude and phase Bode plots for $\phi_{11}(L,s)$ and $\phi_{21}(L,s)$.

3.2.2. Step responses

We analyze the behavior of the system given step inputs $v(0,t) = v_{step}H(t)$ and $q(0,t) = q_{step}H(t)$, where $H(\cdot)$ is the Heaviside function. The step responses are

10

$$v(x,t) = v_{step}\left[e^{-\frac{x}{\lambda_1\tau}}\left(1 - e^{-a\left(t-\frac{x}{\lambda_1}\right)}\right)H\left(t - \frac{x}{\lambda_1}\right) + e^{-a\left(t-\frac{x}{\lambda_2}\right)}H\left(t - \frac{x}{\lambda_2}\right)\right]$$

$$+ \frac{q_{step}}{\rho^*\tau}\left[-e^{-\frac{x}{\lambda_1\tau}}\left(1 - e^{-a\left(t-\frac{x}{\lambda_1}\right)}\right)H\left(t - \frac{x}{\lambda_1}\right) + \left(1 - e^{-a\left(t-\frac{x}{\lambda_2}\right)}\right)H\left(t - \frac{x}{\lambda_2}\right)\right] \quad (34)$$

$$q(x,t) = v_{step}\rho^*\tau a\left[e^{-\frac{x}{\lambda_1\tau}}e^{-a\left(t-\frac{x}{\lambda_1}\right)}H\left(t - \frac{x}{\lambda_1}\right) - e^{-a\left(t-\frac{x}{\lambda_2}\right)}H\left(t - \frac{x}{\lambda_2}\right)\right]$$

$$+ q_{step}\left[e^{-\frac{x}{\lambda_1\tau}}e^{-a\left(t-\frac{x}{\lambda_1}\right)}H\left(t - \frac{x}{\lambda_1}\right) + \left(1 - e^{-a\left(t-\frac{x}{\lambda_2}\right)}\right)H\left(t - \frac{x}{\lambda_2}\right)\right] \quad (35)$$

3.3. Congested flow

Consider now the system in the congestion flow regime. Here we have $\lambda_1 > 0, \lambda_2 < 0$, hence two boundary conditions are needed, one at the upstream boundary and one at the downstream boundary. A plot of the characteristics is shown in Figure 6.
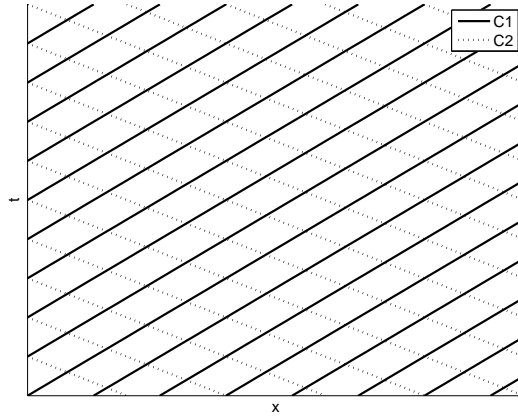

Figure 6: Illustration of the characteristics for supercritical flow, $\lambda_1 > 0, \lambda_2 < 0$.

Using (26) we can write

$$\begin{pmatrix} \hat{\xi}_1(x,s) \\ \hat{\xi}_2(x,s) \end{pmatrix} = \underbrace{\Phi(x,s)\begin{pmatrix} 1 & 0 \\ -\frac{\phi_{21}(L,s)}{\phi_{22}(L,s)} & \frac{1}{\phi_{22}} \end{pmatrix}}_{\Gamma(x,s)}\begin{pmatrix} \hat{\xi}_1(0,s) \\ \hat{\xi}_2(0,s) \end{pmatrix}. \quad (36)$$

with

$$\gamma_{11}(x,s) = e^{-\frac{x}{\lambda_1\tau}}e^{-\frac{sx}{\lambda_1}}, \quad (37a)$$

$$\gamma_{12}(x,s) = 0, \quad (37b)$$

$$\gamma_{21}(x,s) = \alpha\frac{\lambda_1}{\lambda_2}\left(e^{-\frac{x}{\lambda_1\tau}}e^{-\frac{sx}{\lambda_1}} - e^{-\frac{L}{\lambda_1\tau}}e^{-\frac{s}{\lambda_2}\left(x-L\frac{\lambda_1-\lambda_2}{\lambda_1}\right)}\right)\frac{1}{s+\alpha}, \quad (37c)$$

$$\gamma_{22}(x,s) = e^{-\frac{s(x-L)}{\lambda_2}}. \quad (37d)$$

4. Numerical validation

Many phenomena interact in vehicular flow on a freeway. The ARZ equations provide a finer modelling of these dynamics. Studying of the linearized model in the spectral domain brings up a simple framework that paves the way to establishing control strategies for the system. Prior to using such techniques, it is
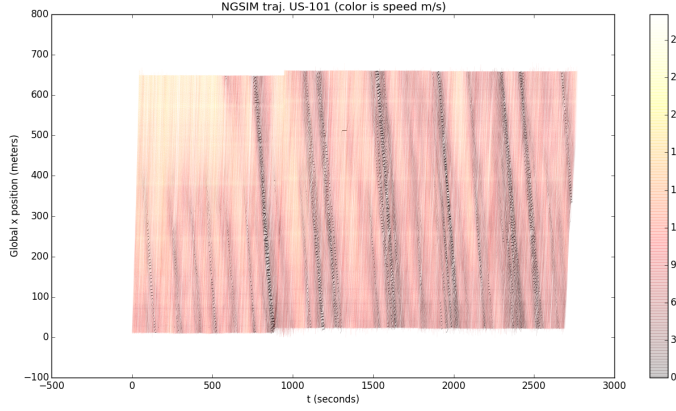
11

Figure 7: NGSIM trajectories (the color represents the measured speed of each car in m/s)

necessary to assess how realistic the model is in its linearized form. This section will subsequently confront the prediction of the model and the actual flow and velocity data gathered in the well known NGSIM data set.

4.1. Data source: NGSIM trajectories

The NSGIM trajectory data set gathers trajectories of vehicles sampled with a 10 Hz frequency thanks to high precision cameras. After converting units to the universal system, each point in the table contains several pieces of information such as **vehicle_ID** (each vehicle has a unique ID), **veh_class** (1 for motorcycle, 2 for cars, 3 for trucks, only cars are taken into account here), **time_since_epoch_ms** (time in ms since epoch timestamp), **local_y** (longitudinal coordinate of the front center of the vehicle with respect to the entry edge of the section in the direction of travel) (meters), **veh_v** (vehicle speed) (meters per second). 45 minutes are recorded on a 650 meter long section. There are five lanes along the section of the freeway under scrutiny which is taken into account when computing the lineic density of vehicles ρ. The trajectories are represented in the (t, x) domain on Figure 7. Only a subset of the spatial domain will be used though because of the presence of ramps that would break the homogeneity of the freeway. The viable domain is 200 meters long.

4.2. Reconstructing (v, q) maps from NGSIM trajectories

The NGSIM does not directly provide the values $v(t, x)$ and $q(t, x)$ in the resolution domain $[0, T] \times [0, L]$. In order to obtain macroscopic quantities out of the microscopic measurements, one divides the time and space grid $[0, T] \times [0, L]$ into small buckets $([i \Delta t, (i+1) \Delta t] \times [j \Delta x, (j+1) \Delta x])_{i \in \{1...n_t\}, j \in \{1...n_x\}}$. Here i corresponds to time and j to space. The operation consists in gathering the corresponding data points into bins and then estimating the quantities of interest in each bin. Let $card$ denote the function that gives the number of elements in a given set i.e. its cardinal.

4.2.1. Binning formulae

The size of each bucket is $\Delta t \times \Delta x$. In each bucket, a certain number of traces are available and ρ, v and q are assumed to be constant. Here several formulae are presented that enable the conversion of a set of records of vehicles' positions into a map of speed, flow and density as a function of time and position.

Binning formula for v:. The speed is assumed to be constant in each bucket. Thus a straightforward estimator for that quantity is the empirical average. Let $\widehat{v}_{i,j}$ the estimator for the speed in bucket (i, j).

$$\widehat{v}_{i,j} = mean_{trace \in bucket_{i,j}} \left(v \left(trace \right) \right)$$

12

Binning formula for ρ:. One considers a bucket with index (i, j). by definition

$$\rho_{i,j} = \frac{1}{n_{lanes}\,\Delta x\,\Delta t} \int\int_{(t,x)\in[i\,\Delta t,\,(i+1)\,\Delta t]\times[j\,\Delta x,\,(j+1)\,\Delta t]} \rho\,(x,t)\,dxdt$$

Any given vehicle will have its position recorded every 0.1 second. Therefore it is also possible to count the number of traces in a given bucket and normalize it by the sampling rate. The contribution of a given vehicle to the density of a bucket is proportional to the number of traces it has left in the bucket. If the speed is assumed to be locally constant, this is proportional to the time this vehicle spends in the bucket and consistent with the conservation of the total number of vehicles across all buckets.

$$\widehat{\rho}_{i,j} = \frac{1}{n_{lanes}\,\Delta x\,\Delta t\,\text{sampling rate}} card\left(\{trace\mid trace\ \in\ bucket\}\right)$$

Binning formula for q:. By definition, $q\,(x,t) = \rho\,(x,t)\,v\,(x,t)$ so a first estimator for q in the bucket (i,j) is logically

$$\widehat{q}_{i,j} = \widehat{v}_{i,j}\widehat{\rho}_{i,j}$$

One can also approximate the flux going through a given bucket $[i\,\Delta t,\,(i+1)\,\Delta t]\times[j\,\Delta x,\,(j+1)\,\Delta t]$ by the number of cars crossing the x coordinate $(j+1)\,\Delta x$ between times $i\,\Delta t$ and $(i+1)\,\Delta t$ normalized by the duration Δt.

If a given vehicle with identification number id_0 crosses $(j+1)\,\Delta x$ between time $i\,\Delta t$ and time $(i+1)\,\Delta t$, then id_0 is present in the bucket $[i\,\Delta t,\,(i+1)\,\Delta t]\times[j\,\Delta x,\,(j+1)\,\Delta t]$ and the bucket $[i\,\Delta t,\,(i+1)\,\Delta t]\times[(j+1)\,\Delta x,\,(j+2)\,\Delta t]$. Therefore, $card\left(\{id\,(trace)\mid trace\in bucket_{i,j}\}\cap\{id\,(trace)\mid trace\in bucket_{i,j+1}\}\right)$ is the number of vehicles that have crossed the coordinate $(j+1)\,\Delta x$ in that interval of time. This gives another estimator of the flux based on counting cars in a straightforward way:

$$\widehat{q}_{i,j}^{count} = \frac{1}{n_{lanes}\Delta t}\,card\left(\{id\,(trace)\mid trace\in bucket_{i,j}\}\cap\{id\,(trace)\mid trace\in bucket_{i,j+1}\}\right)$$
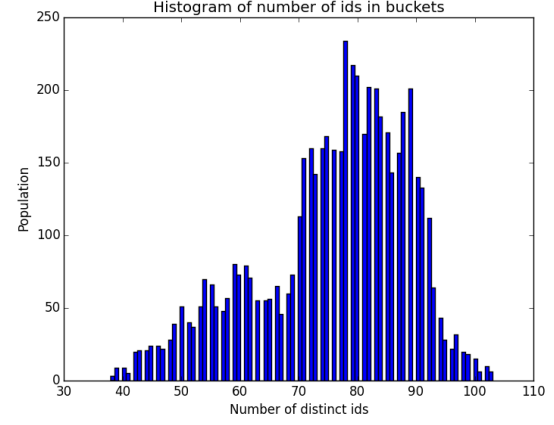
4.2.2. Choosing the number of bins

The discretization grid is $\{[i\,\Delta t,\,(i+1)\,\Delta t]\times[j\,\Delta x,\,(j+1)\,\Delta t]\mid(i,j)\in\{1\ldots N\}\times\{1\ldots N\}\}$. As the estimation formulae above rely on averaging, having a comfortable number of points in each bin provides more stable estimates. It is worth mentioning that usual Central Limit theorem based reasoning for convergence of such estimates is flawed as several samples may correspond to the same vehicle or interacting vehicles, therefore violating the independence assumption of the theorem. Proving the convergence of the estimates above lies clearly beyond the scope of this article and therefore, as a rule of thumb we choose a setup that guarantees that most buckets will host more than 100 traces. This is achieved with a 80×80 grid where the 10th percentile of the number of traces in a given bin is 170. Such a grid also yields a 10th percentile of 56 distinct vehicles per bin. The histograms of number of traces and vehicle per bucket are represented on Figure 8.

4.2.3. Sanity check for the estimators

This article does not provide any theoretical proof of the convergence of the binned estimators for (v, ρ, q) presented above. It is nonetheless possible to check practically that the procedure is coherent. Two estimators are provided for q that use radically different techniques. The first one relies on the average measured speed and the number of traces in a bin. The other one on counting vehicles transiting from a cell to another. Verifying that they both give similar results for a given bucket will therefore confirm that these estimators for q are trustworthy. It will also certify that the estimation technique for ρ is valid. As one can observe on Figure 9, the scatter plot of $\widehat{q}_{i,j}^{count}$ is plotted against $\widehat{q}_{i,j}$ coincides almost perfectly with the line $y = x$ therefore validating the overall binning and estimation procedure.
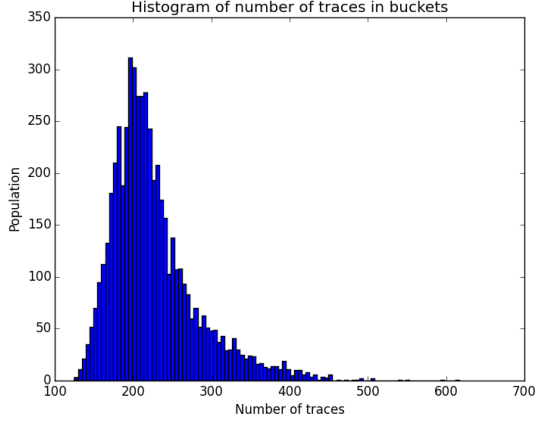
Histogram of number of traces per bucket   Histogram of number of distinct vehicles per bucket

Figure 8: Choice motivation for a 80×80 bucket based discretization grid for the NGSIM data
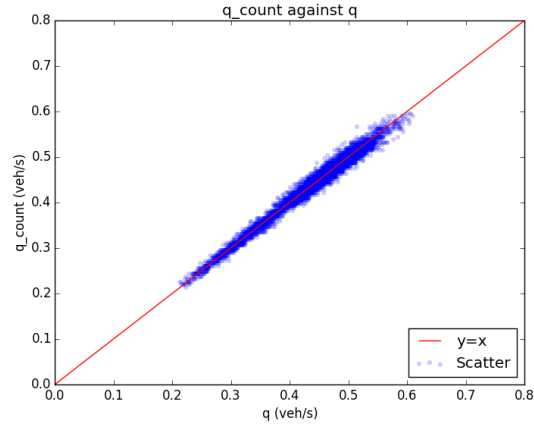

Figure 9: Sanity check for the estimation procedure. $\widehat{q}_{i,j}^{count}$ is plotted against $\widehat{q}_{i,j}$ across the grid of buckets.
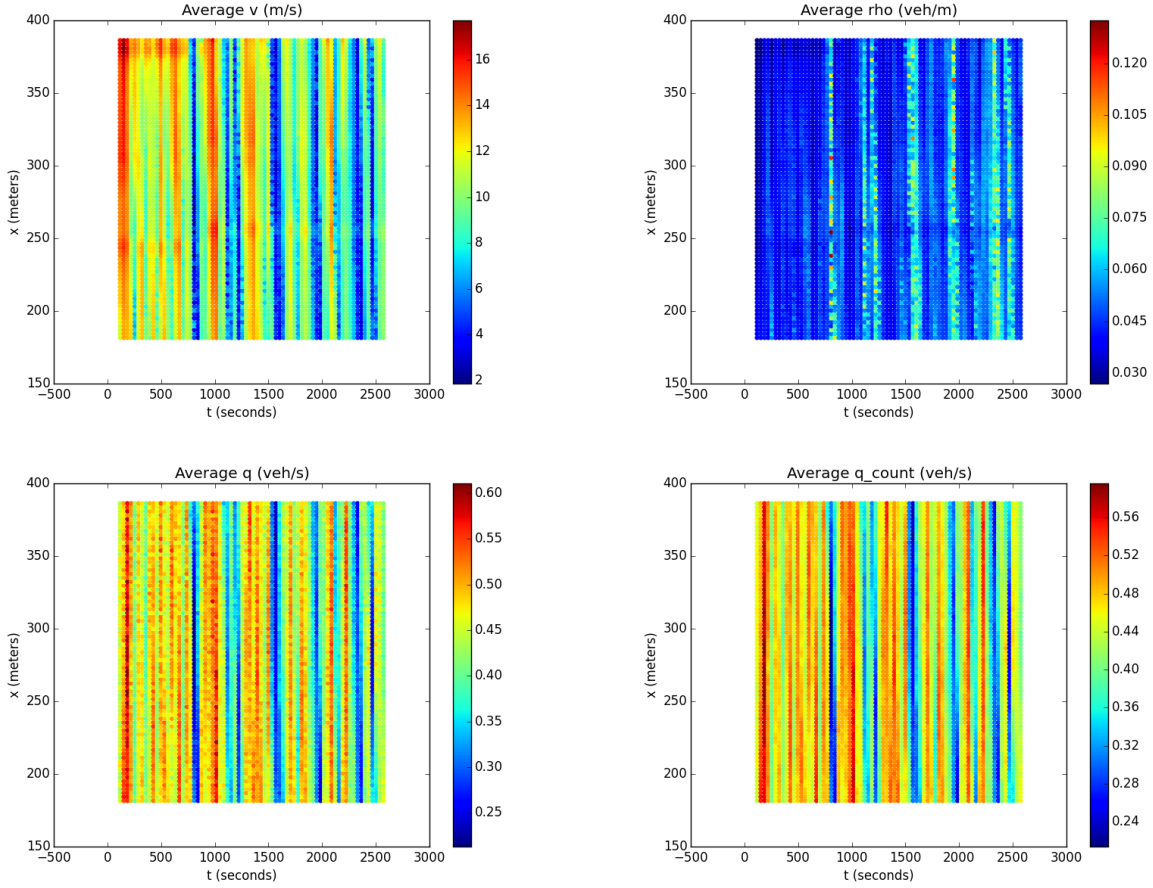
Figure 10: Estimated values for (v, q, ρ). Top left: $\widehat{v}_{i,j}$. Top right: $\widehat{\rho}_{i,j}$. Bottom left: $\widehat{q}_{i,j}$. Bottom right: $\widehat{q}_{i,j}^{count}$.

4.3. Estimated values for (v, q)

In order to check how well the linearized ARZ model fits actual data, one choses a bounded domain and compares the theoretical solution given by the second order model and the data observed. Here we focus one the values of v and q as they correspond to the setup that is the most worth studying. It is also the most directly practical for control. Now that estimates of the actual values of v and q have been designed, they will be used to compute fundamental diagrams and mapped on the $[0, T] \times [0, L]$ domain. Fundamental diagrams will then yield estimates of the eigen values λ_1 and λ_2 that are crucial in this study. Finally, predicted values of v and q will be compared to their measured counterparts which will allow the computation of a fit error. Based on the estimation of this error for different values of the parameter τ, the value offering the best fit will be used as an estimate. Plotting maps of both the predicted values and the observed one will also highlight the phenomena the linearized model accounts for and those it cannot characterize.

4.3.1. Maps

Once the values $\widehat{v}_{i,j}$, $\widehat{\rho}_{i,j}$, $\widehat{q}_{i,j}$, $\widehat{q}_{i,j}^{count}$ have been computed they can be plotted on the discretization grid (see Figure 10). As $\widehat{q}$ and $\widehat{q}^{count}$ give extremely similar results, $\widehat{q}^{count}$ will be used as the estimator of q from now on. Damped oscillations and smoothly decaying values along characteristic lines are the main characteristic the practical implementation of the model should feature.

4.3.2. Fundamental diagrams

From the values that have been estimated it is very straightforward to compute fundamental diagrams as on Figure 11. One of the potential flaws of studying these fundamental diagrams and using them to calibrate
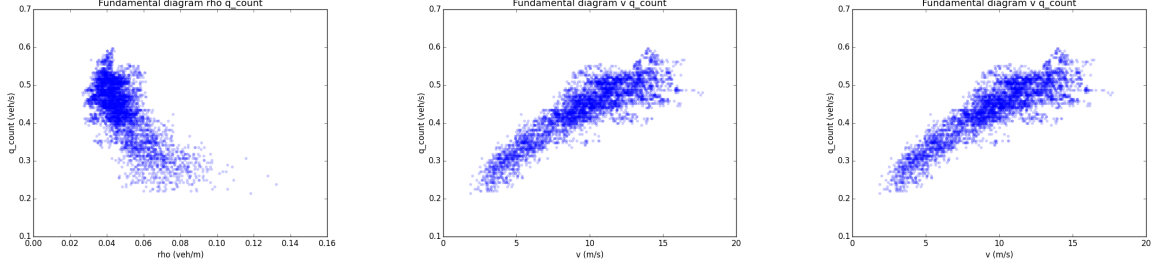
Figure 11: Empirical fundamental diagrams. Left: $\left(\widehat{\rho}, \widehat{q}^{count}\right)$. Middle: $\left(\widehat{v}, \widehat{q}^{count}\right)$. Right: $\left(\widehat{\rho}, \widehat{v}\right)$.

the model's parameters as we do below could come from the fact that the data set is small. Even though many points are collected, they only give information about cars traveling in a small region of time and space. Therefore it is certain that our measurements are highly correlated. This seems to be confirmed by the fact that the fundamental diagrams below only correspond to the congested regime. Most of the points are concentrated about the same region. This is not enough to guarantee that the estimated quantities are reliable. However, NGSIM is to this day one of the most comprehensive data sets of vehicle behavior on a freeway. It is therefore one of the best ways one has to validate that a traffic model is realistic. The fact that most points lie in the same region is also a sign that the linearization hypothesis is reasonable in that context. Observed deviations from the equilibrium are indeed generally small. (The equilibrium, i.e. the linearization point, is estimated below).

4.3.3. Calibration of λ_1 and λ_2, linearization point

$\lambda_1 = v^*$ and $\lambda_2 = Q'(v^*)$ therefore the calibration of λ_1 consists in finding a value of v around which the fundamental diagram (v, q) will be linearized. λ_2 will consist in the estimated slope of the fundamental diagram. λ_2 is estimated with a standard Ordinary Least Squares method. The data set above only corresponds to the congested regime and the fundamental diagram is almost affine.

The method used here is therefore quite straightforward. The estimator for v^* is chosen as the empirical mean of $\widehat{v}_{i,j}$: $\widehat{\lambda}_1 = \widehat{v}^*$. A linear model is fitted: $\widehat{q}^{count} = b_1\widehat{v} + b_0 + \varepsilon$ (where ε represents the noise in the model that would ideally be centered, homoschedastic and uncorrelated but is not practically) and the estimator for λ_2 is then $\widehat{\lambda}_2 = \widehat{b}_1$. q^* is estimated by the empirical average of $\widehat{q}^{count}$ and ρ^* by the ratio of the estimates for q^* and v^*. Provided each estimator is convergent, the continuity of the functional $(x, y) \rightarrow \frac{x}{y}$ on its domain guarantees the convergence of the estimator for ρ^*. The empirical results are presented on Figure 12. The determination coefficient is mediocre, it could be improved by filtering out outliers and more generally by gathering more data. Improving the quality of the estimation will be the subject of further work on that matter. Significance tests for the coefficients of the linear model are not presented. The assumptions they rely on about the linear depency between $\widehat{q}$ and $\widehat{v}$ are clearly not respected here as the noise is auto-correlated. Further work needs to turn this rather heuristic method for estimating parameters into a fully justified statistical procedure. This article focuses is qualitatively assessing what phenomena can be accounted for by the linearized second order model.

4.4. Simulated values for (v, q, ρ)

The data above shows that only the congested regime is to be modeled for the NGSIM data. Therefore the theory developed for the $\lambda_2 < 0$ will be put to use here.

4.4.1. Fourier decomposition of input for a linear PDE

The Partial Differential Equation under scrutiny here is linearized. Therefore, decomposing boundary conditions into a sum and then adding the predicted values inside the domain $[0, T] \times [0, L]$ will give the exact solution. The spectral domain analysis presented above is very useful to that end and will be leveraged thanks to Fourier analysis. Fourier transform is a linear operator that is practically implemented thanks to the Fast Fourier Transform. A real signal $\{f(t) \mid t \in [0, T]\}$ on one of the boundaries $\{(x = 0, t) \mid t \in [0, T]\}$

16
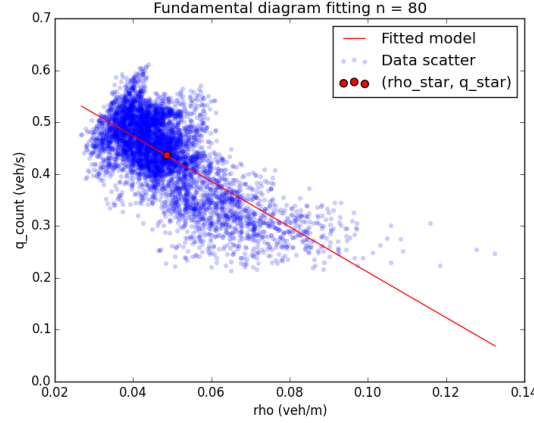
$$\widehat{\lambda}_1 = 8.96 \quad \widehat{\lambda}_2 = -4.37 \quad \widehat{\rho}^* = 0.049 \quad \widehat{v}^* = 8.96 \quad \widehat{q}^* = 0.44 \quad r^2 = 0.48$$

Figure 12: Calibration of λ_1 and λ_2. The figure shows the average point used to compute $\widehat{v}^*$ and $\widehat{q}^*$. The affine model used to estimate λ_2 is also plotted.

or $\{(x = L, t) \mid t \in [0, T]\}$ is transformed into a periodic signal by infinite duplication and then turned into a Fourier series $\{t \to \mu + \sum_{k=1}^n \beta_k \cdot cos\,(k \cdot wt + \phi_k)\,H \mid t \in [0, T]\}$. This process is known to be convergent with an infinite sum for any square integrable function. It is practically extremely accurate in our case even though the FFT only relies on a finite number of Fourier coefficients. For both upstream and downstream boundary conditions, eye inspection cannot distinguish the original signal from its Fourier series decomposition. In Appendix 4.5 the generic way of computing the solution of the PDE inside the inner domain is presented. The process is quite straightforward although the necessary computations are somewhat cumbersome.

4.4.2. Simulated maps

Prior to using Fourier decomposed signals and elementary solutions, it is necessary to convert the data into the diagonalized basis. First of all, the difference with respect to the equilibrium is computed for each bucket: $\widetilde{\widehat{v}}_{i,j} = \widehat{v}_{i,j} - \widehat{v}^*$, $\widetilde{\widehat{q}}_{i,j} = \widehat{q}_{i,j} - \widehat{q}^*$. Once λ_1 and λ_2 have been estimated, estimates for ξ_1 and ξ_2 are computed thanks to the following equations: $\widehat{\xi}_{1_{i,j}} = \frac{\widehat{\rho}^* \widehat{\lambda}_2}{\widehat{\lambda}_1 - \widehat{\lambda}_2} \widetilde{\widehat{v}}_{i,j} + \widetilde{\widehat{q}}_{i,j}$, $\widehat{\xi}_{2_{i,j}} = \frac{\widehat{\rho}^* \widehat{\lambda}_1}{\widehat{\lambda}_1 - \widehat{\lambda}_2} \widetilde{\widehat{v}}_{i,j}$. Then the predicted values for q and v can be computed thanks to the inverse linear transform $\widetilde{q} = \xi_1 - \frac{\lambda_1}{\lambda_2} \xi_2$, $\widetilde{v} = \frac{\lambda_1 - \lambda_2}{\rho^* \lambda_1} \xi_2$. This procedure gives comparison maps for the data and predicted values for both the (v, q) and the (ξ_1, ξ_2) domains. Figure 13 shows important qualitative properties of the model. First of all, as expected, the model generally predicts with a very good accuracy the decay of all quantities along their characteristic lines. This is a realistic feature that cannot be paralleled by first order models. The general quality of the fit is rather good with most of the error on v and q in a 20 percent range of the data's amplitude between minimum and maximum values. What is also quite satisfactory is that the linearized second order model manages to capture oscillations observed on the boundary and account for their decay accurately. The value of τ used to compute the plots below is described in 4.4.3.

4.4.3. Calibration of τ

For each value of τ one computes the mean absolute error (MAE). That is to say, the average difference in absolute value between what is simulated and what is predicted for each discretization bucket. v and q are not physically homogeneous, therefore it is not sensible to aggregate the errors over these quantities. However, ξ_1 and ξ_2 are both expressed in veh/s. Summing their MAE gives a reliable uni-dimensional index of the quality of the fit with respect to τ. This quantity is computed for different values of τ ranging from 5 to 80 seconds. The value offering the best fit is $\tau^* = 39.18$.

17
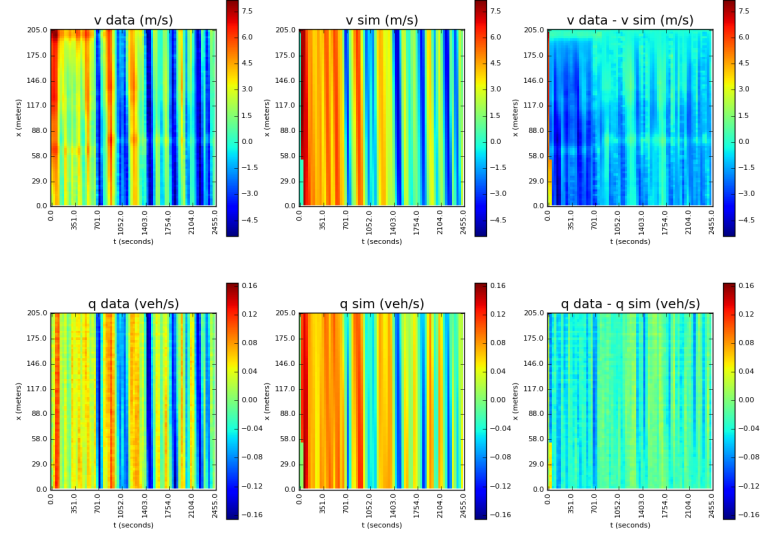
Top row: q. Bottom row: v.
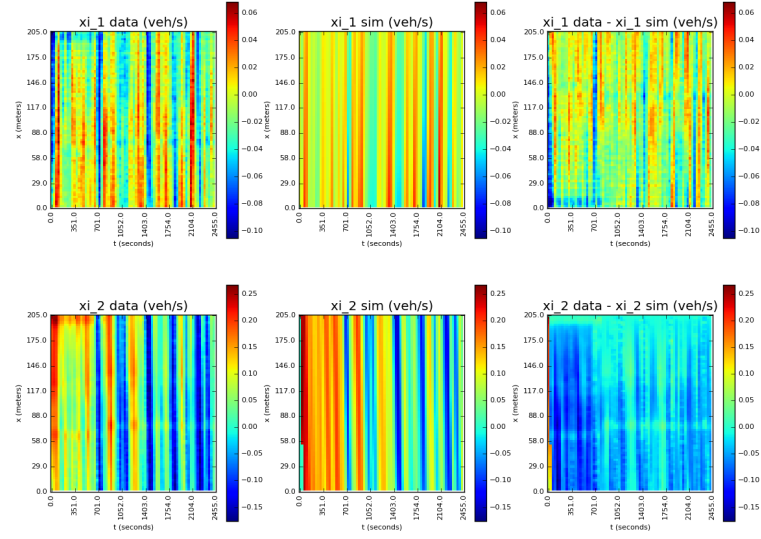
Top row: ξ_1. Bottom row: ξ_2.

Figure 13: Data versus predicted. Top: (v, q) domain. Bottom: (ξ_1, ξ_2) domain. First column: data. Middle column: predictions. Third column: prediction - data.
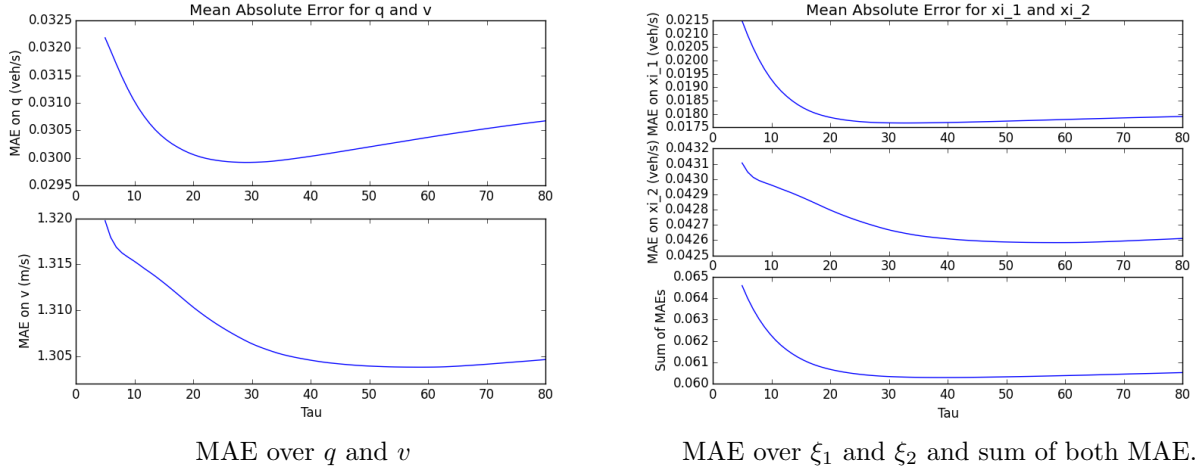
MAE over q and v MAE over ξ_1 and ξ_2 and sum of both MAE.

Figure 14: Calibration of τ, one minimizes the sum of MAE over ξ_1 and ξ_2.

4.5. Generic computations for time domain to Laplace domain transforms and vice versa

The aim is to derive the time domain responses of generic input signals such as $t \to H(t)$ and $t \to \cos(wt + \phi) H(t)$ when multiplied in the Laplace domain by $\frac{1}{s+\alpha}$. This then enables the computation of any response that decomposes in a Fourier transform.

4.5.1. Step function input

The time domain input function is $H(t)$. One computes the inverse Laplace transform of $s \to \frac{1}{s(s+\alpha)}$ which is

$$t \to \frac{1}{\alpha} \left(1 - e^{-\alpha t}\right) H(t)$$

4.5.2. Phased cosine input

The time domain input function is $\cos(wt + \phi) H(t)$. One computes the inverse Laplace transform of $s \to \frac{1}{s+\alpha} \left\{ \frac{s}{s^2+\omega^2} \cos(\phi) - \frac{w}{s^2+w^2} \sin(\phi) \right\}$ which can be directly achieved in the time domain. Indeed, the result is given by the convolution product $t \to \left(e^{-\alpha \cdot} H(\cdot) \star \cos(\omega \cdot + \phi) H(\cdot)\right)(t)$, that is to say

$$t \to \frac{-e^{-\alpha \cdot t} \left(\alpha \cdot \cos(\phi) + w \cdot \sin(\phi)\right) + \alpha \cdot \cos(wt + \phi) + w \cdot \sin(wt + \phi)}{\alpha^2 + w^2} H(t) = \kappa_{\alpha,w,\phi}^{cos}(t)$$

4.5.3. Fourier sum input

Let the input be $t \to \mu H(t) + \sum_{k=1}^{n} \beta_k \cdot \cos(k \cdot wt + \phi_k) H(t)$. The time domain response is therefore

$$t \to \frac{\mu}{\alpha} \left(1 - e^{-\alpha t}\right) H(t) + \sum_{k=1}^{n} \beta_k \cdot \kappa_{\alpha,w,\phi}^{cos}(t)$$

4.6. Fourier decomposition and time domain responses for $\lambda_2 > 0$

Let $\alpha = -\frac{\lambda_2}{\tau(\lambda_1 - \lambda_2)} < 0$. Let $H(t)$ the Heaviside function.

$$\begin{pmatrix} \widehat{\xi_1}(x,s) \\ \widehat{\xi_2}(x,s) \end{pmatrix} = \Phi(x,s) \begin{pmatrix} \widehat{\xi_1}(0,s) \\ \widehat{\xi_2}(0,s) \end{pmatrix}$$

with

$$\Phi(x,s) = \begin{bmatrix} e^{-\frac{sx}{\lambda_1}} e^{-\frac{x}{\lambda_1 \tau}} & 0 \\ -\alpha \frac{\lambda_1}{\lambda_2} \left(e^{-\frac{sx}{\lambda_1}} e^{-\frac{x}{\lambda_1 \tau}} - e^{-\frac{sx}{\lambda_2}}\right) \frac{1}{s+\alpha} & e^{-\frac{sx}{\lambda_2}} \end{bmatrix}$$

implies the following fundamental responses for the system.

4.6.1. Fundamental responses in time domain:

- $\begin{pmatrix} \xi_1(0,t) \\ \xi_2(0,t) \end{pmatrix} = \begin{pmatrix} H(t) \\ 0 \end{pmatrix}$:

  - $\xi_1(x,t) = e^{-\frac{x}{\lambda_1 \tau}} H\left(t - \frac{x}{\lambda_1}\right)$

  - $\xi_2(x,t) = -\frac{\lambda_1}{\lambda_2}\left(e^{-\frac{x}{\lambda_1\tau}}\left(1 - e^{-\alpha\left(t-\frac{x}{\lambda_1}\right)}\right) H\left(t - \frac{x}{\lambda_1}\right) - \left(1 - e^{-\alpha\left(t-\frac{x}{\lambda_2}\right)}\right) H\left(t - \frac{x}{\lambda_2}\right)\right)$

- $\begin{pmatrix} \xi_1(0,t) \\ \xi_2(0,t) \end{pmatrix} = \begin{pmatrix} 0 \\ H(t) \end{pmatrix}$:

  - $\xi_1(x,t) = 0$

  - $\xi_2(x,t) = H\left(t - \frac{x}{\lambda_2}\right)$

- $\begin{pmatrix} \xi_1(0,t) \\ \xi_2(0,t) \end{pmatrix} = \begin{pmatrix} \cos(\omega t + \phi) \\ 0 \end{pmatrix}$:

  - $\xi_1(x,t) = e^{-\frac{x}{\lambda_1\tau}} \cos\left(\omega\left(t - \frac{x}{\lambda_1}\right) + \phi\right) H\left(t - \frac{x}{\lambda_1}\right)$

  - $\xi_2(x,t) = -\frac{\lambda_1\alpha}{\lambda_2}\left(e^{-\frac{x}{\lambda_1\tau}} \kappa_{\alpha,\omega,\phi}^{cos}\left(t - \frac{x}{\lambda_1}\right) - \kappa_{\alpha,\omega,\phi}^{cos}\left(t - \frac{x}{\lambda_2}\right)\right)$

- $\begin{pmatrix} \xi_1(0,t) \\ \xi_2(0,t) \end{pmatrix} = \begin{pmatrix} 0 \\ \cos(\omega t + \phi) \end{pmatrix}$:

  - $\xi_1(x,t) = 0$

  - $\xi_2(x,t) = \cos\left(\omega\left(t - \frac{x}{\lambda_2}\right) + \phi\right) H\left(t - \frac{x}{\lambda_2}\right)$

4.7. Fourier decomposition and time domain responses for $\lambda_2 < 0$

This time, $\alpha = -\frac{\lambda_2}{\tau(\lambda_1 - \lambda_2)} > 0$.

$$\begin{pmatrix} \widehat{\xi}_1(x,s) \\ \widehat{\xi}_2(x,s) \end{pmatrix} = \Phi(x,s) \begin{pmatrix} \widehat{\xi}_1(0,s) \\ \widehat{\xi}_2(L,s) \end{pmatrix}$$

with

$$\Gamma(x,s) = \begin{pmatrix} e^{-\frac{sx}{\lambda_1}} e^{-\frac{x}{\lambda_1\tau}} & 0 \\ \alpha\frac{\lambda_1}{\lambda_2}\left(e^{-\frac{x}{\lambda_1\tau}} e^{-\frac{sx}{\lambda_1}} - e^{-\frac{L}{\lambda_1\tau}} e^{-\frac{s}{\lambda_2}\left(x - L\frac{\lambda_1 - \lambda_2}{\lambda_1}\right)}\right)\frac{1}{s+\alpha} & e^{-\frac{s(x-L)}{\lambda_2}} \end{pmatrix}$$

implies the following fundamental responses for the system.

4.7.1. Fundamental responses in time domain

- $\begin{pmatrix} \xi_1(0,t) \\ \xi_2(L,t) \end{pmatrix} = \begin{pmatrix} H(t) \\ 0 \end{pmatrix}$:

  - $\xi_1(x,t) = e^{-\frac{x}{\lambda_1\tau}} H\left(t - \frac{x}{\lambda_1}\right)$

  - $\xi_2(x,t) = \frac{\lambda_1}{\lambda_2}\left(e^{-\frac{x}{\lambda_1\tau}}\left(1 - e^{-\alpha\left(t-\frac{x}{\lambda_1}\right)}\right) H\left(t - \frac{x}{\lambda_1}\right) - e^{-\frac{L}{\lambda_1\tau}}\left(1 - e^{-\alpha\left(t - \frac{x - L\frac{\lambda_1-\lambda_2}{\lambda_1}}{\lambda_2}\right)}\right) H\left(t - \frac{x - L\frac{\lambda_1-\lambda_2}{\lambda_1}}{\lambda_2}\right)\right)$

- $\begin{pmatrix} \xi_1(0,t) \\ \xi_2(L,t) \end{pmatrix} = \begin{pmatrix} 0 \\ H(t) \end{pmatrix}$:

    – $\xi_1(x,t) = 0$

    – $\xi_2(x,t) = H\left(t - \frac{x-L}{\lambda_2}\right)$

- $\begin{pmatrix} \xi_1(0,t) \\ \xi_2(L,t) \end{pmatrix} = \begin{pmatrix} \cos(\omega t + \phi) \\ 0 \end{pmatrix}$:

    – $\xi_1(x,t) = e^{-\frac{x}{\lambda_1 \tau}} \cos\left(\omega\left(t - \frac{x}{\lambda_1}\right) + \phi\right) H\left(t - \frac{x}{\lambda_1}\right)$

    – $\xi_2(x,t) = \frac{\lambda_1 \alpha}{\lambda_2}\left(e^{-\frac{x}{\lambda_1 \tau}} \kappa^{cos}_{\alpha,\omega,\phi}\left(t - \frac{x}{\lambda_1}\right) - e^{-\frac{L}{\lambda_1 \tau}} \kappa^{cos}_{\alpha,\omega,\phi}\left(t - \frac{x-L\frac{\lambda_1-\lambda_2}{\lambda_1}}{\lambda_2}\right)\right)$

- $\begin{pmatrix} \xi_1(0,t) \\ \xi_2(L,t) \end{pmatrix} = \begin{pmatrix} 0 \\ \cos(\omega t + \phi) \end{pmatrix}$:

    – $\xi_1(x,t) = 0$

    – $\xi_2(x,t) = \cos\left(\omega\left(t - \frac{x-L}{\lambda_2}\right) + \phi\right) H\left(t - \frac{x-L}{\lambda_2}\right)$

5. Conclusion

In this article we have shown how to use linearization of second order traffic model so as to characterize important properties of the system such as Riemann Invariants. In particular time domain responses predict in the free-flow regime that the system is unstable and traffic waves would see their amplitude increase at an exponential rate before the system drifts away from the equilibrium point. This is a strong result that sheds a new light on traffic oscillations. In the congested regime such oscillatory phenomena are also present as we have shown in our numerical experiments. The new method of analysis and its spectral form will later on make any control strategy easy to set up. The higher realism of the ARZ model as compared to LWR will enable efficient traffic regulation on freeways thank to varying speed limits and on-ramp metering. It will also avoid resonating with jamitons. Further work needs to focus on designing such traffic optimization schemes. Numerically, new methods for macroscopic variable estimation have been developed that are reliable practically. Although it is still necessary to prove the convergence of this estimation procedure and which resolution should be used for such tasks. It is interesting to see that, thanks to the spectral resolution of the problem, the choice of the grid size is then driven by statistical convergence and not by CFL conditions.

References

[1] D. Schrank, B. Eisele, , T. Lomax, Urban mobility report, Tech. rep., Texas A and M Transportation Institute (2012).

[2] M. J. Lighthill, J. B. Whitham, On kinematic waves. II: A theory of traffic flow on long crowded roads., Proc. Royal. Soc. (1955) 317–345.

[3] P. I. Richards, Shock waves on the highway, Operations Research 4 (1) (1956) pp. 42–51.

[4] S. K. Godunov, A difference scheme for numerical solution of discontinuous solution of hydrodynamic equations, Math. Sbornik 47 (1969) 271–306.

[5] S. Osher, Riemann solvers, the entropy condition, and difference, SIAM Journal on Numerical Analysis 21 (2) (1984) 217–235. `doi:10.1137/0721016`.

[6] C. F. Daganzo, The cell transmission model: A dynamic representation of highway traffic consistent with the hydrodynamic theory, Transportation Research Part B: Methodological 28 (4) (1994) 269–287.

[7] C. F. Daganzo, The cell transmission model, part ii: network traffic, Transportation Research Part B: Methodological 29 (2) (1995) 79–93.

[8] C. Daganzo, Requiem for second-order fluid approximations of traffic flow, Transportation Res. Part B 29 (4) (1995) 277–286.

[9] Y. Sugiyama, M. Fukui, M. Kikuchi, K. Hasebe, A. Nakayama, K. Nishinari, S. ichi Tadaki, S. Yukawa, Traffic jams without bottlenecks, experimental evidence for the physical mechanism of the formation of a jam, New J. Phys.`doi:doi:10.1088/1367-2630/10/3/033001`.

[10] M. R. Flynn, A. R. Kasimov, J. c. Nave, R. R. Rosales, B. Seibold, On jamitons, self-sustained nonlinear traffic waves (2008).

[11] M. R. Flynn, A. R. Kasimov, J. c. Nave, R. R. Rosales, B. Seibold, Self-sustained nonlinear waves in traffic flow, Physical Review E (2009) 056113.

[12] B. Seibold, M. R. Flynn, A. R. Kasimov, R. Ruben Rosales, Constructing set-valued fundamental diagrams from jamiton solutions in second order traffic models, ArXiv e-prints`arXiv:1204.5510`.

[13] B. A. Zielke, R. L. Bertini, M. Treiber, Empirical measurement of freeway oscillation characteristics: an international comparison, Transportation Research Record: Journal of the Transportation Research Board 2088 (1) (2008) 57–67.

[14] M. Mauch, M. J. Cassidy, Freeway traffic oscillations: Observations and predictions, in: In Proc. 15th Int. Symp. on Transportation and Traffic Theory, Elsevier, 2002, pp. 653–674.

[15] B. Coifman, S. Krishnamurthy, X. Wang, Lane-change maneuvers consuming freeway capacity, in: S. Hoogendoorn, S. Luding, P. Bovy, M. Schreckenberg, D. Wolf (Eds.), Traffic and Granular Flow 03, Springer Berlin Heidelberg, 2005, pp. 3–14. `doi:10.1007/3-540-28091-X_1`.
URL `http://dx.doi.org/10.1007/3-540-28091-X_1`

[16] S. Ahn, C. M. J., Freeway traffic oscillations and vehicle lane-change maneuvers, Transportation and traffic theory 2007 : papers selected for presentation at ISTTT17, a peer reviewed series since 1959. (2007) 691–710.

[17] H. J. Payne, Models of Freeway Traffic and Control, Simulation Councils, Incorporated, 1971.

[18] G. B. Whitham, Linear and Nonlinear Waves, A Wiley-Interscience publication, Wiley, 1974.

[19] G. F. Newell, Nonlinear effects in the dynamics of car following, Operations Research 9 (2) (1961) pp. 209–229.
URL `http://www.jstor.org/stable/167493`

[20] H. Zhang, A theory of nonequilibrium traffic flow, Transportation Research Part B: Methodological 32 (7) (1998) 485 – 498. `doi:http://dx.doi.org/10.1016/S0191-2615(98)00014-9`.
URL `http://www.sciencedirect.com/science/article/pii/S0191261598000149`

[21] A. Aw, M. Rascle, Resurrection of second order models of traffic flow, SIAM Journal of Applied Mathematics 60 (3) (2000) 916–938.

[22] H. M. Zhang, A non-equilibrium traffic model devoid of gas-like behavior, Transportation Res. Part B 36 (2002) 275–290.

[23] M. Rascle, An improved macroscopic model of traffic flow: derivation and links with the lighthill-whitham model, Mathematical and computer modelling 35 (2002) 581–590.

[24] J.-P. Lebacque, S. Mammar, H. Haj-Salem, The aw-rascle and zhang's model: Vacuum problems, existence and regularity of the solutions of the riemann problem, Transportation Research Part B: Methodological 41 (7) (2007) 710 – 721. `doi:http://dx.doi.org/10.1016/j.trb.2006.11.005`.
URL `http://www.sciencedirect.com/science/article/pii/S0191261507000112`

[25] S. Moutari, M. Rascle, A hybrid lagrangian model based on the aw-rascle traffic flow model, SIAM Journal on Applied Mathematics 68 (2) (2007) 413–436. `arXiv:http://dx.doi.org/10.1137/060678415`, `doi:10.1137/060678415`.
URL `http://dx.doi.org/10.1137/060678415`

[26] J.-P. Lebacque, S. Mammar, H. H. Salem, Generic second order traffic flow modelling, in: Transportation and Traffic Theory 2007. Papers Selected for Presentation at ISTTT17, 2007.

[27] F. Berthelin, P. Degond, M. Delitala, M. Rascle, A model for the formation and evolution of traffic jams, Archive for Rational Mechanics and Analysis 187 (2) (2008) 185–220.

[28] S. Fan, M. Herty, B. Seibold, Comparative model accuracy of a data-fitted generalized aw-rascle-zhang model, Networks and Heterogeneous Media 9 (2) (2014) 239–268.

[29] S. Mammar, J.-P. Lebacque, H. H. Salem, Riemann problem resolution and godunov scheme for the aw-rascle-zhang model, Transportation Science 43 (4) (2009) 531–545. `arXiv:http://dx.doi.org/10.1287/trsc.1090.0283`, `doi:10.1287/trsc.1090.0283`.
URL `http://dx.doi.org/10.1287/trsc.1090.0283`

[30] J. M. Greenberg, Congestion redux, SIAM J. Appl. Math 64 (2004) 1175–1185.

[31] D. Chen, J. Laval, Z. Zheng, S. Ahn, A behavioral car-following model that captures traffic oscillations, Transportation Research Part B: Methodological 46 (6) (2012) 744 – 761. `doi:http://dx.doi.org/10.1016/j.trb.2012.01.009`.

[32] Z. Zheng, S. Ahn, D. Chen, J. Laval, Freeway traffic oscillations: Microscopic analysis of formations and propagations using wavelet transform, Procedia - Social and Behavioral Sciences 17 (0) (2011) 702 – 716, papers selected for the 19th International Symposium on Transportation and Traffic Theory. `doi:http://dx.doi.org/10.1016/j.sbspro.2011.04.540`.

[33] X. Litrico, V. Fromion, Modeling and control of hydrosystems, Springer, 2009.

[34] A. Hofleitner, C. Claudel, A. Bayen, Reconstruction of boundary conditions from internal conditions using viability theory, in: American Control Conference, IEEE, 2012, pp. 640–645.